

Cover Page



Universiteit Leiden



The handle <http://hdl.handle.net/1887/21863> holds various files of this Leiden University dissertation.

Author: Fayolle, Edith Carine

Title: From ice to gas : constraining the desorption processes of interstellar ices

Issue Date: 2013-10-01

Linking the ice content and gas abundances of organic molecules in massive young stellar objects

Abstract. Sources of complex organic molecules display a large chemical diversity, including small-scale differentiation between nitrogen and oxygen bearing complex species. We aim to test whether complex chemical differences can be explained by different initial ice conditions in different lines of sight.

We use the IRAM 30m and the Submillimeter Array to search for complex organic molecules in three massive young stellar objects (MYSOs) with known ice abundances, but without luminous hot cores, to expand the existing sample of MYSOs with both ice and complex gas observations.

Complex molecules are detected toward all three MYSOs at comparable abundances with respect to CH_3OH as in classical hot core sources. The N-bearing molecules are generally concentrated toward the source center, while most O- and C-bearing molecules are present both in the center and in the colder envelope. $\text{HNCO}/\text{CH}_3\text{OH}$ gas ratios tentatively depend on the $\text{OCN}^-/\text{CH}_3\text{OH}$ and $\text{NH}_3/\text{CH}_3\text{OH}$ ice ratios, while $\text{CH}_3\text{CN}/\text{CH}_3\text{OH}$ gas ratios do not. This is consistent with new model predictions. Both theory and observations suggest that gas temperature and initial abundances are important factors for complex organic distributions toward MYSOs. To quantify their relative impact requires a large spatially resolved survey of YSOs with ice detections.

E. C. Fayolle, K. I. Öberg, R. T. Garrod, E. F. van Dishoeck and S. E. Bisschop
in preparation

7.1 Introduction

Organic molecules containing more than 6 atoms, so-called complex organics (Herbst & van Dishoeck 2009), are commonly found in the warm and dense gas phase ($T > 100$ K, $n > 10^6$ cm⁻³) around young stellar objects (YSOs) (e.g. Blake et al. 1987; Cazaux et al. 2003; Fuente et al. 2005). Abundances and abundance ratios of complex organics are found to vary substantially between (Helmich & van Dishoeck 1997) and within YSOs (e.g. Wyrowski et al. 1999), suggestive of formation and/or destruction routes that are highly environment specific as well as a possible variation in chemical initial conditions. The potential dependencies together with the fact that complex organics present large numbers of lines, spanning most excitation conditions found in space, entails that these molecules have a great potential to provide useful clues on the physical conditions where they are found, as well as the chemical and physical history (Nomura & Millar 2004). Complex molecules are also of high interest for origins of life theories since they are the precursors of even more complex prebiotic material (Ehrenfreund & Charnley 2000). Molecular probe development and advancements in prebiotic evolution from organics rely both on a detailed understanding of complex organic chemistry. The formation and destruction mechanisms of most complex organics and the corresponding process efficiencies are, however, poorly constrained.

The formation of organic molecules around massive YSOs (MYSOs) was first thought to proceed through gas phase reactions in dense hot cores, following evaporation of ice grain mantles (e.g. Charnley et al. 1992). Recent laboratory experiments and modeling efforts point now toward a more complicated sequential scenario which relies to a greater extent on surface formation routes on sub-micron sized dust particles. Herbst & van Dishoeck (2009) classified complex organic molecules in terms of generations according to the following scenario: In interstellar clouds and in the deeply embedded early phases of star formation, atoms and molecules accrete or form on the surface of dust grains, building up an icy mantle of simple species like H₂O, CH₄, NH₃ (Tielens & Hagen 1982). This icy molecular mantle is processed at low temperature by atoms, which can diffuse even at the low temperatures in cloud cores, creating the 0th generation of organic molecules. A good example of this species is CH₃OH, which is efficiently formed at low temperature by the hydrogenation of CO ice (Watanabe & Kouchi 2002; Watanabe et al. 2003, 2004; Fuchs et al. 2009; Cuppen et al. 2009). 1st generation complex organics form during heating up the cold envelope by the increasing luminosity of the central source and is due to a combination of photo-processing of the ice - resulting in radical production - and a warming up (20 to 100 K) of the grains - enhancing mobility of radicals and molecules (Garrod et al. 2008; Öberg et al. 2010). When the icy grains move inward and reach a regions warmer than 100 K, the icy mantle evaporates, bringing the 0th and 1st generation organics into the gas phase, where additional chemical reactions give rise to the formation of the 2nd generation complex organics (e.g. Charnley et al. 1992; Viti et al. 2004, Doty et al. 2002).

In the proposed scenario of complex molecule formation, the initial ice mantle plays a critical role. The exact composition of this ice may therefore have a large effect both on the product composition of formed organics and on their overall formation efficiency. Garrod et al. (2008) and Öberg et al. (2009a) find for example that CH₃OH

ice is a key starting point for most complex organic formation. Rodgers & Charnley (2001) have shown that the relative amount of NH_3 in the ice has a large impact on the $\text{CH}_3\text{CN}/\text{CH}_3\text{OH}$ abundance ratio in the protostar using a hot core chemistry model. Observationally testing these relationships would provide key constraints on the formation pathways of complex organic molecules.

Isolated MYSOs with warm inner envelopes are good laboratories to test this hypothesis as these sources are bright enough to observe a wide variety of organics and some of them present ice feature from the cold outer protostellar envelope (Gibb et al. 2004). Sources presenting both complex gas and ice features are, however, rare as the sources need to be evolved to possibly display a bright hot core chemistry and young enough such that the ice material has not been completely consumed by accretion, warm up and envelope-dispersal. In the massive YSO sample studied by Bisschop et al. (2007), only three hot cores present ice spectra. Such a small number prevents any analysis of correlation between ice and gas content and motivates our search for other objects displaying both ice features and gas phase organics.

To extend the sample of sources with both complex organics and ice observations, we propose to explore the presence of gas phase organics species around massive young sources with available ice observations, but without that a bright hot core phase. Massive objects NGC7538 IRS9, W3 IRS5, and AFGL490 have been observed in the mid-infrared by ISO and analyzed for ice abundances by Gibb et al. (2004). NGC7538 IRS9 is a $6 \times 10^4 L_\odot$ luminous object located in Perseus. It is close to hot core source NGC7538 IRS1 and displays at least 3 bipolar outflows, shows evidence for accretion (Sandell et al. 2005) as well as a hot component close to the central object. W3 IRS5 is associated with five young stellar objects, two of which are massive (van der Tak et al. 2005; Megeath et al. 2005; Rodón et al. 2008; Chavarría et al. 2010). It has a luminosity of $17 \times 10^4 L_\odot$ and presents strong S-bearing molecular lines. AFGL490 is a very young medium-mass YSO of $4.6 \times 10^3 L_\odot$, in transition to an Herbig Be star, which drives a high-velocity outflow (Mitchell et al. 1995) and shows evidence of a rotating disk (Schreyer et al. 2006). These three objects are considered to be at a different evolution stage compared to the hot-core sources and it is unclear a priori what level of complex organic activity is expected and where in the protostellar envelope any detected emission originates.

In this study we use a combination of single dish IRAM 30m data and spatially resolved observations from the Submillimeter Array¹ to search for organic molecules around these three MYSOs and report on their complex organic abundances in the cool protostellar envelope and in a warmer region closer to the star. A subset of this data was used in the Öberg et al 2013 (in press) to study the radial distribution of molecules in NGC7538 IRS9, while the present study focuses on the overall detection rate of organics in these weak-line sources, and chemical connections to the initial ice chemistry and to traditional hot core sources. The chapter is organized as follow: the observations are described in Section 7.2, the results of the line analysis is shown in Sections 7.3.1, 7.3.2 and 7.3.3. The chemistry in our sample is compared to the chemistry in

1. The Submillimeter Array is a joint project between the Smithsonian Astrophysical Observatory and the Academia Sinica Institute of Astronomy and Astrophysics. It is funded by the Smithsonian Institute and the Academia Sinica.

traditional hot-core sources in Section 7.3.4. Section 7.3.5 presents correlation studies between ice and gas column densities and abundances, testing the impact of initial ice compositions on the complex chemistry. A discussion on the use of these line-poor sources to underpin the origins of complex chemistry is presented in Section 7.4, which is followed by the conclusions of this study.

7.2 Observations and Analysis

7.2.1 Observations

Table 7.1: Source characteristics and ice abundances

Source	d kpc	L $10^4 L_{\odot}$	$N_{\text{H}_2\text{O}}$ 10^{17} cm^{-2}	X / % $N_{\text{H}_2\text{O}}$			
				CH_3OH	CH_4	NH_3	OCN^-
NGC7538 IRS9	2.7	3.5	70	4.3 ± 0.6	2 ± 0.4	15 ± 2.7	1.7 ± 0.5
W3 IRS5	2.0	17	51	<3.3	<1.3	<5.7	<0.23
AFGL490	1.4	0.46	6.2	11 ± 4	<2.4	<16	<1.2
W33A	3.8	5.3	110	14 ± 4	1.5 ± 0.2	15 ± 4	6.3 ± 1.9
AFGL2591	3.3	18	12	14.2 ± 2	<2.7	<2.3	–
NGC7538 IRS1	2.4	15	22	<4	1.5 ± 0.5	<17	<0.5
Orion IRc2	4	1.0	24.5	10 ± 3	–	–	2 ± 0.6
G24.78	7.7	1.2	–	–	–	–	–
G75.78	1.9	19	–	–	–	–	–
NGC6334 IRS1	1.7	11	–	–	–	–	–

The MYSOs NGC7538 IRS9, W3 IRS5, and AFGL490 located in Perseus NGC7538 at 2.7 kpc, in Perseus W3 at 2.0 kpc and in Camelopardalis OB1 at 1.4 kpc respectively (see Table 7.1) have been observed with the IRAM 30m and the Submillimeter Array (SMA).

NGC7538 IRS9 was observed with the IRAM 30m telescope on February 19–20, 2012 using the EMIR 230 GHz receiver and the new FTS backend. The two sidebands cover 223–231 GHz and 239–247 GHz at a spectral resolution of $\sim 0.2 \text{ km s}^{-1}$ and with a sideband rejection of -15dB (Carter et al. 2012). Pointing was checked every 1–2 hours and found to be accurate within 2–3". Focus was checked every 4 hours, and generally remained stable through most of the observations, i.e. corrections on the order of 0.2–0.4" were common, but a correction of 0.7" was required once. Spectra were acquired in both position switching and wobbler switching modes. The resulting spectra had similar relative line intensities, indicative of no emission in the wobbler off position. The wobbler switching mode was considerably more stable and these data alone are used for the quantitative analysis. The raw IRAM spectra were converted to main beam temperatures and fluxes using forward and beam efficiencies and antenna temperature to flux conversion values listed at www.iram.es/IRAMES/mainWiki/Iram30mEfficiencies. The spectra were reduced using CLASS. A global baseline was fitted to each 4 GHz spectral chunk using 4–7 windows. The individual scans were baseline subtracted and

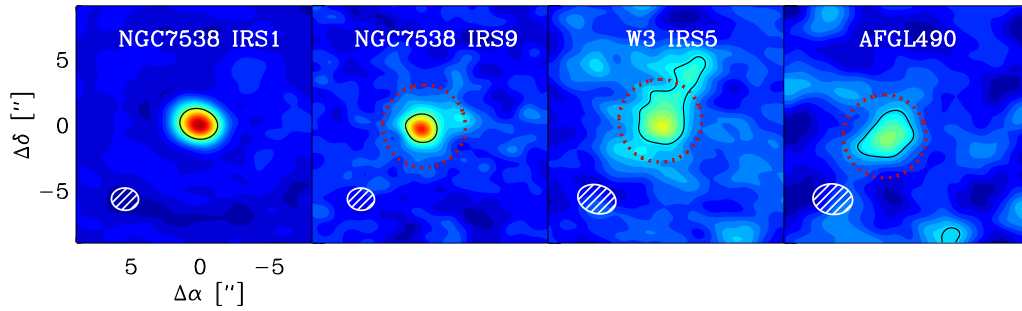


Figure 7.1: Image of the CH_3CN emission using the 239.138 GHz line acquired by the SMA for NGC7538 IRS1, NGC7538 IRS9, W3 IRS5, and AFGL490. The black contour presents the 50 % line intensity, and the synthesized beam is shown in white at the bottom left. A 2'' radius mask is over plotted in dashed red which is used to extract spectra.

averaged. The absolute flux scale of the lines were then set using calibrated SMA data as outlined in detail by Öberg et al (in press).

SMA observations were acquired in the compact and extended array configurations. The data in the compact configuration were taken on the 15th of October 2011 for all sources and with 7 antennas, resulting in baselines between 16 - 77 m. The data in the extended configuration were obtained using 8 antennas, resulting in 44 - 226 m baselines and were acquired on the 29th of July 2011 for W3 IRS5 and AFGL490 and on the 15th of August 2011 for NGC7538 IRS9. The SMA correlator was set-up to obtain a spectral resolution of $\sim 1 \text{ km s}^{-1}$ using 128 channels for each of the 46 chunks covering 227-231 GHz in the lower sideband and 239-243 GHz in the upper sideband. The $\tau_{225\text{GHz}}$ was 0.09 on the 29th of July, 0.1 on the 15th of August, and 0.07 on the 15th of October 2011.

The MIR package has been used to perform the first data reduction steps (flux calibration and continuum subtraction). Absolute flux calibration has been done with Calisto and band pass calibrators were 1924-292 and 3c84 for the compact observations, and 3c454.3 and 3c279 were used for the 29th of July and 15th of July observations respectively. Gain calibrators for NGC7538 IRS9 include 0014+612 and 0102+584, and the objects 0244+624, 0359+509, and 0102+584 have been used for W3 IRS5 and AFGL490. The compact and extended data were combined for each source with MIRIAD using natural weighting, which resulted in synthesized beam sizes of $2.0'' \times 1.7''$ for NGC 7538 IRS 9, $2.2'' \times 2.8''$ for W3 IRS5, and $2.3'' \times 2.9''$ for AFGL490.

7.2.2 Spectral extraction and rms

Both the IRAM and SMA data have been frequency calibrated using the bright 5-4 CH_3OH ladder around 241.7 GHz, correcting for the intrinsic velocity of the different sources. The SMA spectra are extracted using a 2'' mask around the center phase of each source. The mask dimension is chosen to encompass all CH_3CN line emission at 239.318 GHz that can be associated with a centrally condensed component, as shown

in Figure 7.1.

The rms for the IRAM and SMA observation of each source has been derived by determining the standard deviation in a line free region of several hundred channels: the 229.37-229.445 GHz region for the lower side band and the 240.7 - 240.75 GHz region for the upper side band. The rms derived for these very deep IRAM observations is between 15 and 20 mK. For the SMA data, the rms for the lower side band is ~ 70 mK, and ~ 100 mK for the upper side-band.

7.3 Results

7.3.1 Line identification and characterization

Figure 7.2 shows the 239-243 GHz spectral region for the three targeted line-poor MYSOs and the traditional hot-core source NGC7538 IRS1 using the IRAM 30m. The MYSOs present a lower line density as well as some line overlaps with the traditional hot core. Lines from complex organics listed by Bisschop et al. (2007) found in traditional hot-core sources were searched for in the MYSOs spectra. CH_3OH , CH_3CN , CH_3CCH , HNCO , CH_3OCH_3 , and CH_3CHO lines were identified in at least one of the MYSOs using the splatalogue catalogue tool and the CDMS and the JPL spectral databases (Müller et al. 2001; Pickett et al. 1998). All available lines in the observed spectral range have been used for the quantitative analysis except for CH_3OH where only the lines from the 5-4 ladder are used to simplify the excitation analysis.

Identified lines are fitted with a Gaussian function in IDL using the routine `gaussfit` for isolated lines and `mpfitfun` when a multiple gaussian fit was required because of overlapping lines. A local baseline component was added to the fits when needed and the presented uncertainties are output by the fitting routines. 3σ upper limits are calculated using average FWHM for the different sources. Unresolved multiplets are treated in one out three ways depending on the nature of the overlapping lines: 1) if one of the possible contributing lines has a very low Einstein coefficient or high upper energy level and that a line presenting the same characteristics elsewhere in the spectrum is not clearly resolved, then it is discarded and only the rest of the multiplet is fitted 2) if the lines are coming from the same species and the upper energy level and Einstein coefficients are identical or close to identical, then the degeneracies are added and the feature is treated as a single line, 3) if none of the two previous conditions are met, the multiplet is discarded.

Line upper energy levels, Einstein coefficients, degeneracies from Splatalogue are listed together with derived line intensities and FWHM in Table 7.2 for CH_3OH from the single dish observation, in Table 7.3 for CH_3OH from the SMA spectra, in Table 7.4 for CH_3CN , in Table 7.5 for CH_3CCH and Table 7.6 for HNCO , CH_3OCH_3 and CH_3CHO . No other complex molecules were detected towards any of the sources. For molecules with weak lines, only the IRAM data have been used since the SMA observations have lower spectral resolution and a higher rms.

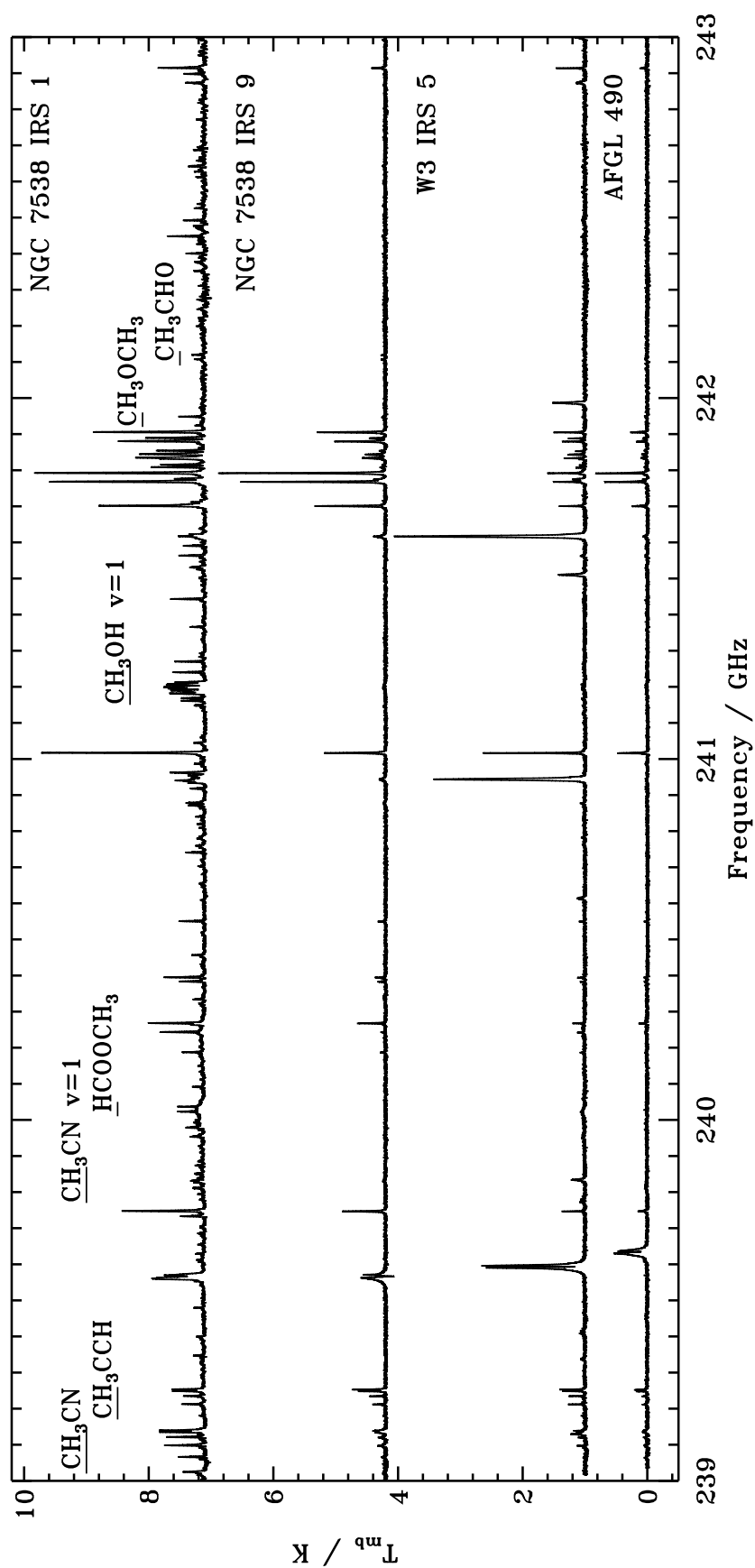


Figure 7.2: The 239-243 GHz spectral window from the IRAM 30m displaying emission lines for typical hot core source NGC 7538 IRS 1 and weak line MYSOs NGC7538 IRS9, W3IRS5, AFGL490.

Table 7.2: CH₃OH lines data from IRAM 30m spectra.

Freq (GHz)	E_{up} (K)	log A	g_u	NGC7538 IRS9		W3 IRS5		AFGL490	
				$\int T_{mb}dV$ (K)	FHWM (km s ⁻¹)	$\int T_{mb}dV$ (K)	FHWM (km s ⁻¹)	$\int T_{mb}dV$ (K)	FHWM (km s ⁻¹)
239.746	49.1	-4.25	11	4.08±0.05	3.70±0.03	1.21±0.03	2.32±0.04	0.91±0.04	4.4±0.2
241.700	47.9	-4.22	11	6.08±0.05	3.47±0.02	1.41±0.03	2.43±0.04	1.33±0.04	3.53±0.07
241.767	40.4	-4.24	11	11.97±0.04	3.37±0.01	2.20±0.04	2.98±0.03	3.30±0.04	3.11±0.02
241.791	34.8	-4.22	11	13.65±0.04	3.37±0.01	2.49±0.04	2.91±0.03	4.00±0.03	3.09±0.02
241.807	115.2	-4.66	22	0.45±0.06	4.5±0.4	0.32±0.03	1.58±0.09	<0.27	-
241.813	122.7	-4.66	11	0.21±0.05	3.6±0.6	0.23±0.03	1.7±0.2	<0.27	-
241.830	130.8	-4.66	11	<0.21	-	0.26±0.03	2.0±0.2	<0.27	-
241.833	84.6	-4.41	22	2.62±0.05	4.61±0.06	1.09±0.03	2.18±0.04	0.71±0.05	4.9±0.2
241.842	72.5	-4.29	11	2.00±0.08	5.5±0.1	0.63±0.04	1.90±0.08	0.52±0.06	6.8±0.5
241.844	82.5	-4.41	11	0.48±0.06	3.3±0.3	0.64±0.04	2.2±0.1	0.29±0.03	3.50±0.02
241.852	97.5	-4.41	11	0.64±0.06	5.5±0.4	0.44±0.03	2.1±0.1	0.30±0.05	6.5±0.8
241.879	55.9	-4.22	11	4.64±0.05	3.64±0.02	1.32±0.04	2.58±0.05	1.02±0.04	4.1±0.1
241.888	72.5	-4.29	11	1.68±0.05	4.28±0.09	0.75±0.03	2.04±0.06	0.50±0.05	5.2±0.3
241.904	60.7	-4.29	11	3.14±0.02	3.66±0.02	0.98±0.02	2.57±0.03	0.76±0.02	3.85±0.07
241.905	57.1	-4.30	11	3.14±0.02	3.66±0.02	0.98±0.02	2.57±0.03	0.76±0.02	3.85±0.07

Table 7.3: CH₃OH lines extracted from SMA observation from the 2'' radius compact region.

Freq (GHz)	E _{up} (K)	logA	g _u	NGC7538 IRS9		W3 IRS5		AFGL490	
				∫T _{mb} dV (K)	FHWM (km s ⁻¹)	∫T _{mb} dV (K)	FHWM (km s ⁻¹)	∫T _{mb} dV (K)	FHWM (km s ⁻¹)
239.746	49.1	-4.25	11	10.1± 0.5	4.6± 0.2	3.1± 0.4	1.9± 0.2	4.0± 0.5	4.6± 0.5
241.700	47.9	-4.22	11	9.6± 0.4	4.1± 0.2	3.6± 0.4	2.4± 0.2	4.8± 0.6	5.9± 0.5
241.767	40.4	-4.24	11	10.7± 0.4	3.5± 0.1	4.2± 0.4	2.3± 0.2	2.3± 0.4	2.6± 0.3
241.791	34.8	-4.22	11	9.3± 0.4	3.16± 0.09	4.6± 0.5	2.9± 0.2	3.1± 0.5	4.9± 0.7
241.807	115.2	-4.66	22	2.7± 0.6	6± 1	1.8± 0.5	2.4± 0.5	< 1.5	-
241.813	122.7	-4.66	11	1.3± 0.4	3.6± 0.9	1.3± 0.5	2.8± 0.8	< 1.5	-
241.830	130.8	-4.66	11	<1.1	-	<1.4	-	< 1.5	-
241.833	84.6	-4.41	22	8.4± 0.6	4.7± 0.3	4.0± 0.5	2.9± 0.3	2.4± 0.5	4.6± 0.8
241.852	97.5	-4.41	11	2.5± 0.5	3.4± 0.5	1.8± 0.5	1.5± 0.4	< 1.5	-
241.879	55.9	-4.22	11	7.2± 0.4	3.4± 0.2	3.4± 0.4	2.3± 0.2	2.5± 0.5	4.7± 0.7
241.888	72.5	-4.29	11	6.0± 0.5	5.2± 0.3	2.1± 0.4	1.6± 0.2	2.4± 0.7	7± 2
241.904	60.7	-4.29	11	6.9± 0.3	4.5± 0.1	2.2± 0.2	2.2± 0.2	2.2± 0.3	5.2± 0.5
241.905	57.1	-4.30	11	6.9± 0.3	4.5± 0.1	2.2± 0.2	2.2± 0.2	2.2± 0.3	5.2± 0.5

Table 7.4: CH₃CN lines data from IRAM 30m spectra.

Freq (GHz)	E _{up} (K)	logA	g _u	NGC7538 IRS9		W3 IRS5		AFGL490	
				∫T _{mb} dV (K)	FHWM (km s ⁻¹)	∫T _{mb} dV (K)	FHWM (km s ⁻¹)	∫T _{mb} dV (K)	FHWM (km s ⁻¹)
239.023	258.9	-3.00	54	0.31± 0.07	9± 2	< 0.2	-	<0.3	-
239.064	194.6	-2.97	54	0.4± 0.1	9± 2	0.17 ± 0.05	6 ± 2	0.23± 0.05	6± 2
239.096	144.6	-2.95	108	1.04± 0.05	6.0± 0.3	0.44± 0.04	2.2± 0.2	0.48± 0.08	8 ± 1
239.120	108.9	-2.94	54	0.88± 0.05	5.7± 0.3	0.34± 0.04	2.8± 0.3	0.29± 0.07	6± 2
239.133	87.5	-2.93	54	1.14± 0.05	4.6± 0.2	0.47± 0.03	2.4± 0.2	0.42± 0.05	4.9± 0.5
239.138	80.3	-2.93	54	1.46± 0.05	5.2± 0.2	0.52± 0.03	2.1± 0.2	0.47± 0.05	5.4± 0.5

Table 7.5: CH₃CCH lines data from IRAM 30m spectra.

Freq (GHz)	E _{up} (K)	logA	g _u	NGC7538 IRS9		W3 IRS5		AFGL490	
				∫T _{mb} dV (K)	FHWM (km s ⁻¹)	∫T _{mb} dV (K)	FHWM (km s ⁻¹)	∫T _{mb} dV (K)	FHWM (km s ⁻¹)
239.029	439.8	-4.97	58	< 0.21	-	< 0.14	-	< 0.19	-
239.088	346.1	-4.07	16	< 0.21	-	< 0.14	-	< 0.19	-
239.179	201.7	-4.88	58	0.19± 0.05	3.4± 0.6	0.17± 0.05	2.5± 0.6	<0.19	-
239.211	151.1	-4.00	16	0.92± 0.04	3.1± 0.2	0.78± 0.03	2.00± 0.06	0.29± 0.04	3.5± 0.4
239.234	115.0	-4.85	58	1.00± 0.04	2.71± 0.08	0.72± 0.03	1.98± 0.07	0.30± 0.04	3.0± 0.3
239.248	93.3	-4.84	58	1.77± 0.04	2.92± 0.05	1.15± 0.03	2.2± 0.05	0.53± 0.03	2.3± 0.1
239.252	86.1	-4.84	58	2.01± 0.04	2.74± 0.04	1.26± 0.03	2.12± 0.04	0.73± 0.03	2.9± 0.1

Table 7.6: HNCO, CH₃CHO, and CH₃OCH₃ lines data from the IRAM 30m spectra and HNCO acid line data from the SMA 2'' radius compact region.

Species	Freq (GHz)	E _{up} (K)	logA	g _u	NGC7538 IRS9 ∫T _{mb} dV (K)	FWHM (km s ⁻¹)	W3 IRS5 ∫T _{mb} dV (K)	FWHM (km s ⁻¹)	AFGL490 ∫T _{mb} dV (K)	FWHM (km s ⁻¹)
HNCO	240.876	112.6	-3.72	23	0.46±0.08	13±2	0.41±0.05	5.5±0.5	<0.19	-
	241.704	239.9	-3.74	23	<0.21	-	<0.22	-	<0.19	-
	241.708	239.9	-3.74	23	<0.21	-	<0.22	-	<0.19	-
	241.774	69.6	-3.71	23	0.38±0.05	2.7±0.3	0.86±0.05	3.8±0.2	0.22±0.04	2.7±0.4
	242.640	113.1	-3.71	23	<0.21	-	0.49±0.06	8.9±0.8	<0.19	-
SMA	240.876	112.6	-3.72	23	<1.4	-	<1.4	-	<1.3	-
	241.774	69.6	-3.71	23	4.2±0.5	5.8±0.6	5.7±0.6	5.2±0.4	<1.3	-
	242.640	113.1	-3.71	23	2.4±0.6	10±2	<1.4	-	<1.3	-
CH ₃ OCH ₃	225.599	69.8	-3.88	450	0.34±0.04	4.2±0.4	0.12±0.04	2.6±0.6	0.29±0.07	8±2
	240.985	26.3	-3.99	154	<0.22	-	<0.15	-	<0.25	-
	241.529	26.3	-3.99	198	<0.22	-	<0.15	-	<0.21	-
	241.947	81.1	-3.78	378	0.22±0.06	3.5±0.8	0.07±0.02	1.2±0.3	0.25±0.07	6±2
	223.650	72.3	-3.41	50	0.22±0.03	2.8±0.3	<0.18	-	<0.19	-
CH ₃ CHO	223.660	72.2	-3.41	50	0.28±0.04	3.2±0.3	<0.18	-	<0.19	-
	226.552	71.4	-3.39	50	0.29±0.03	2.9±0.3	<0.18	-	<0.19	-
	226.593	71.3	-3.39	50	0.33±0.04	3.5±0.3	<0.18	-	<0.19	-
	229.775	61.5	-4.29	46	<0.19	-	<0.18	-	<0.19	-
	230.302	81.0	-3.38	50	0.20±0.03	2.5±0.3	<0.18	-	<0.19	-
	230.316	81.1	-3.38	50	0.19±0.03	2.3±0.3	<0.18	-	<0.19	-
	242.118	83.8	-3.30	54	0.28±0.04	3.7±0.5	<0.18	-	<0.19	-
	244.789	83.1	-3.29	54	0.24±0.04	3.7±0.5	<0.18	-	<0.19	-
	244.832	83.1	-3.29	54	0.24±0.07	4.2±0.9	<0.18	-	<0.19	-
	244.854	72.3	-4.19	50	<0.19	-	<0.18	-	<0.19	-
242.106	83.9	-3.30	54	0.22±0.05	2.6±0.5	<0.18	-	<0.19	-	

7.3.2 Spatial origin of the line emission

Figures 7.3, 7.4, and 7.5 present the line fluxes of key molecules from both the single-dish observation and the extracted spectra from the SMA observations of the inner regions around the 3 MYSOs. In the higher signal-to-noise ratio (SNR) spectra in Fig. 7.3, the IRAM spectra are clearly not a scaled up versions of the SMA spectra for any of the targeted molecules. This puts qualitative constraints on the origin of the emission from the different molecules. CH_3CN emission from the IRAM and SMA overlap, indicative that most CH_3CN emission originates at the source center, while CH_3CCH flux from the IRAM is not recovered by the SMA, indicative of extended emission. CH_3OH lines display a mixed behavior; lines with higher upper energies show more overlap between the IRAM 30m and SMA spectra than the colder lines. The HNC line flux is very similar for NGC7538 IRS9 and W3 IRS5, but none of the IRAM 30m flux is recovered by the AFGL490 SMA observations, and this molecule thus seems to be present at different scales in different sources.

In Fig. 7.5 the SNR is generally lower, but it is still clear that CH_3CHO toward NGC7538 IRS9 only has extended emission since none of the IRAM 30m line flux is recovered in the SMA spectra. No CH_3CHO lines are detected in the other two MYSOs in the spectral range where IRAM 30m and SMA observations overlap. CH_3OCH_3 is detected toward NGC7538 IRS9 and AFGL490, and in both cases tentative SMA detections suggest that the emission originates from the source centers. Based on the different emission patterns, the molecules found in these spectra are classified as follows: CH_3CCH and CH_3CHO are envelope organics, CH_3CN and CH_3OCH_3 are core organics and CH_3OH and HNC are intermediate cases with significant core and envelope contributions.

7.3.3 Rotational temperature, and column densities

The core and envelope classifications based on spatial emission patterns should be reflected in the rotational temperatures of the different molecules. Rotational diagrams were constructed for molecules with sufficient number of line detections, i.e. CH_3OH (extracted from IRAM and SMA), CH_3CN , CH_3CCH , according to the method described in Goldsmith & Langer (1999). A 10% uncertainty was added to the line integrated area (not listed in the line tables) to account for the fact that the line shapes are not necessarily Gaussian. We used the `linfit` routine in IDL to derive the rotational temperatures as well as the column densities and the routine returned the corresponding uncertainties.

Table 7.7 presents the column densities and rotational temperatures derived for these molecules. The beam-averaged CH_3OH column densities and rotational temperatures derived from the IRAM 30m spectra are in agreement with those found by van der Tak et al. (2000) using the JCMT single dish telescope, including higher frequency lines. The rotational temperature and column densities derived for CH_3OH from the SMA data are always higher than those derived by the IRAM 30m, consistent with that the SMA observations probe material closer to the MYSO center. The third row of Table 7.7 presents the derived temperatures and column densities for CH_3CN

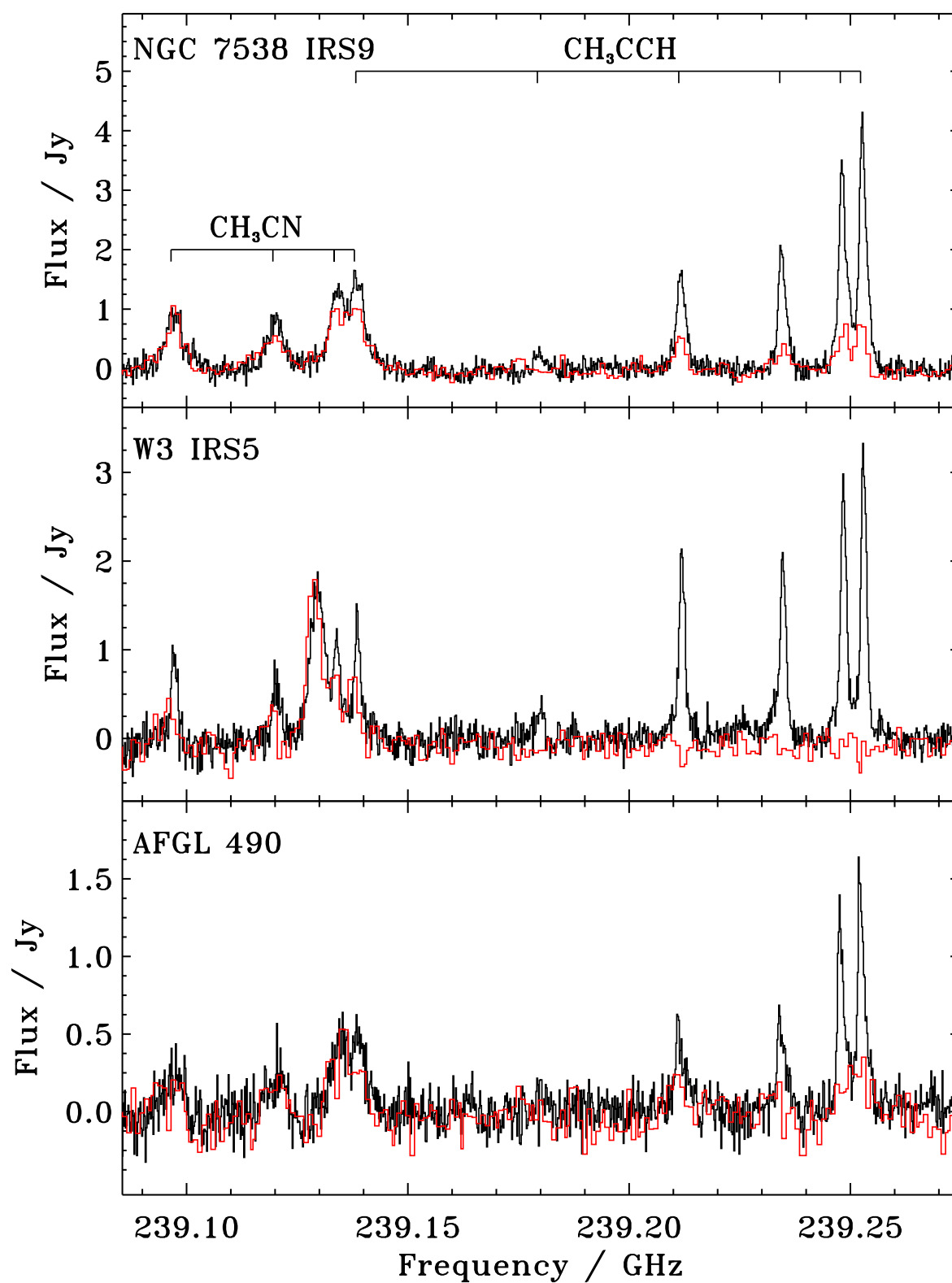


Figure 7.3: Spectral window with several CH₃CN and CH₃CCH lines from the single dish (black lines) and the 2'' interferometric data (red line).

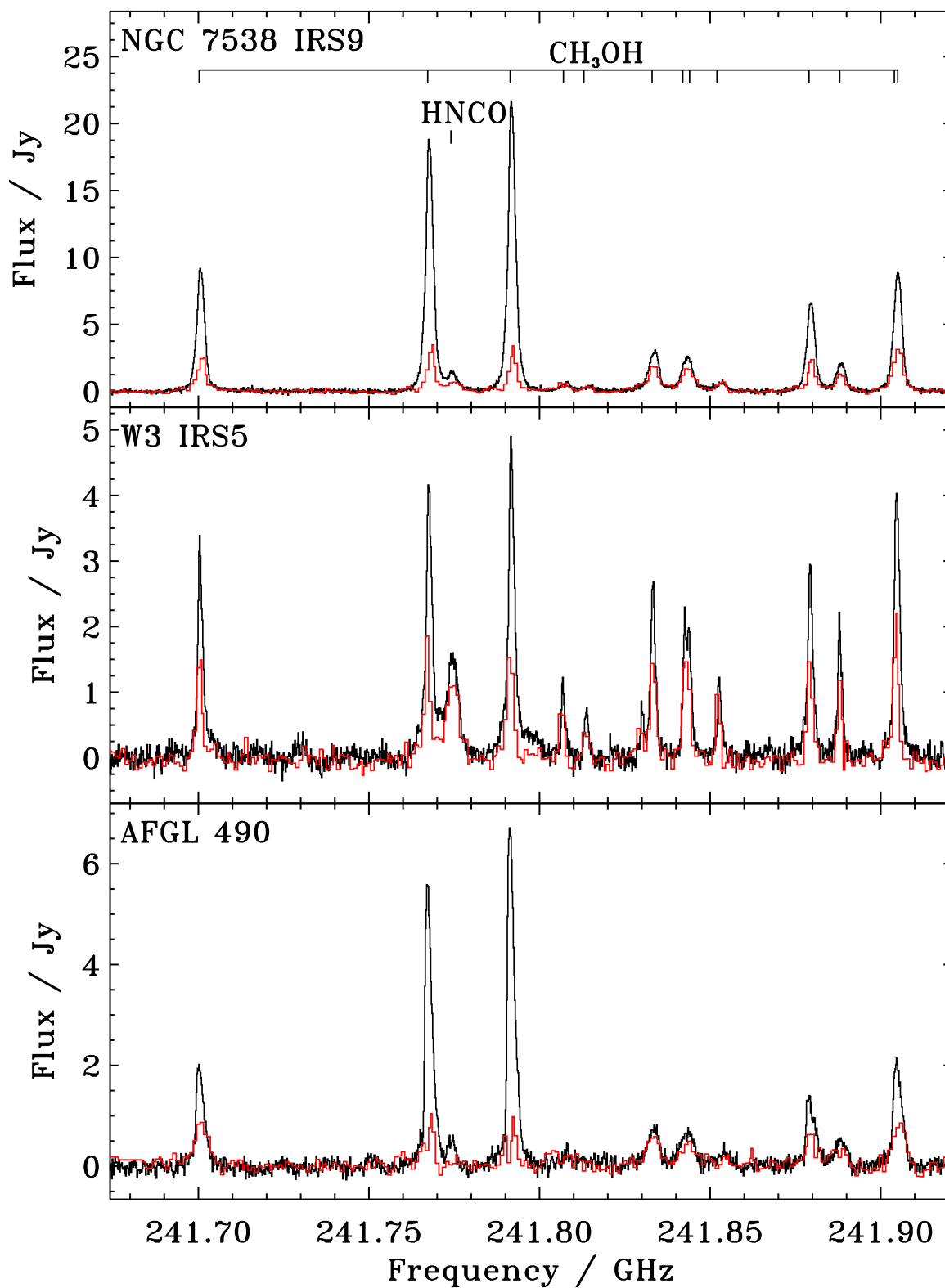


Figure 7.4: Spectral window with several CH₃OH lines from the single dish (black lines) and the 2'' interferometric data (red line).

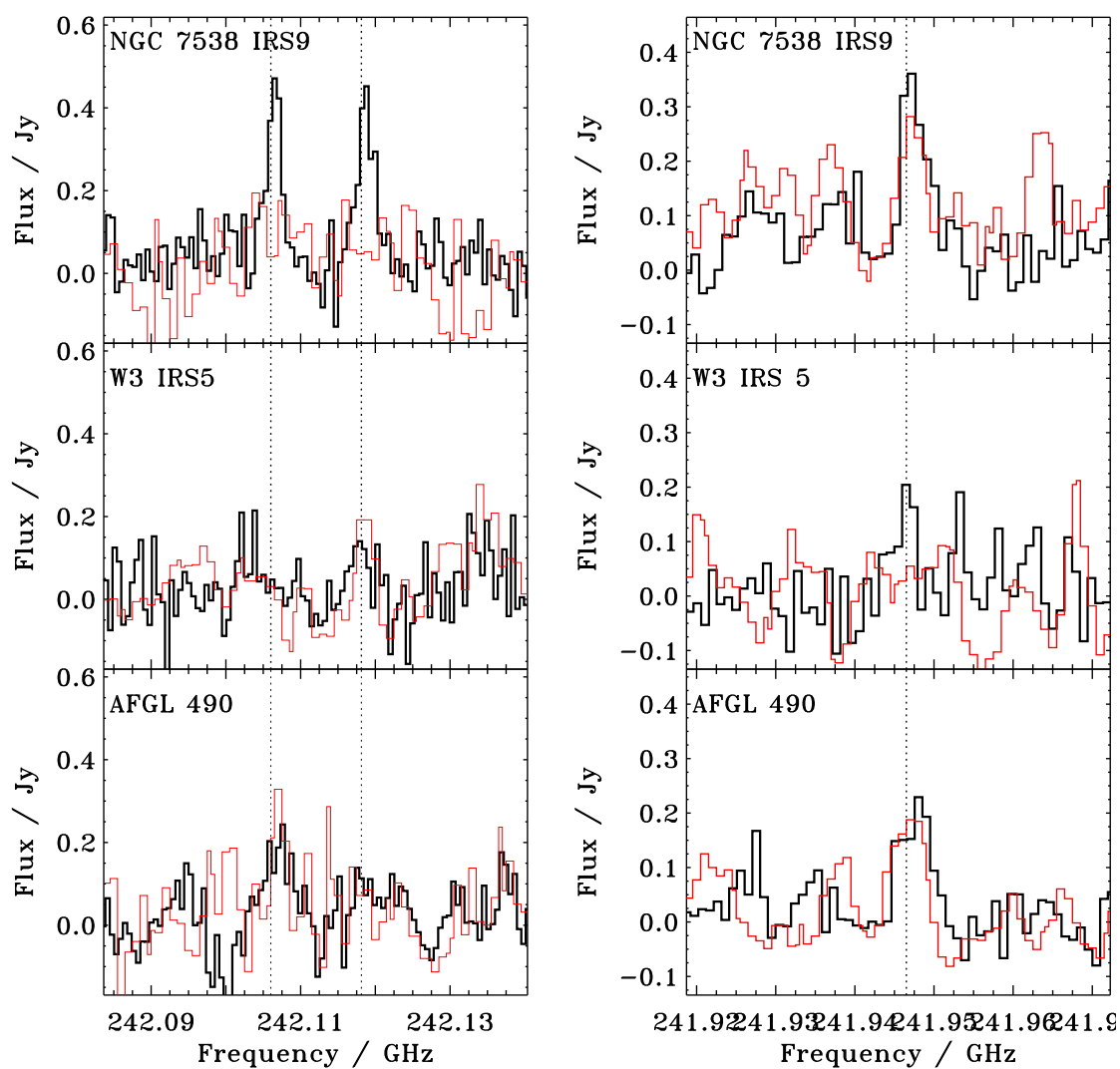


Figure 7.5: Spectra of two CH_3CHO lines at 242.106 GHz and 242.118 GHz (left panel) and the CH_3OCH_3 line at 241.946 GHz (right panel) from the single dish (black line) and $2''$ interferometric data (red line). The three line frequencies are marked by black dotted line.

from the IRAM data assuming that the emission is only coming from the 2'' radii encompassed by the SMA beam, i.e. we apply a dilution factor of 0.16 to account for the SMA extraction mask area (2'' radius) to IRAM beam (5'' radius) ratio. This assumption is justified by the hot-core like rotational temperatures of 80–110 K toward the different MYSOs, which are also consistent with the CH₃OH excitation temperature derived from the SMA spectra. The IRAM data are used here since they present much higher spectral resolution and SNR, and the beam dilution factor is motivated by the observed overlap between the IRAM and SMA line fluxes (see Figure 7.3). The last row shows the rotational temperatures and column densities obtained for the CH₃CCH 14-13 ladder from the IRAM spectra. The rotational temperature of ~50 K toward all sources is consistent with an envelope origin, but suggests that it is mainly present in the luke-warm envelope regions rather than the outermost cold region.

For HNCO, CH₃CHO and CH₃OCH₃, no rotational diagrams can be build due to the very small upper level energy range of the observed transitions, and column densities are calculated using the envelope temperature (the CH₃OH IRAM 30m rotational temperature) if the molecule was classified as an envelope molecule, the core temperature (the CH₃CN rotational temperature) if the molecule was classified as a core molecule, and both rotational excitation temperatures if the molecule is classified as intermediate. For core molecules, the same dilution factor as for CH₃CN was applied (see Table 7.8). For molecules with multiple line detections, the column densities are derived by averaging the individual column densities found for each detected line and taking as uncertainty the square root of the sum of the individual uncertainties squared. Only the IRAM data are used to calculate these column densities since these data present a better SNR.

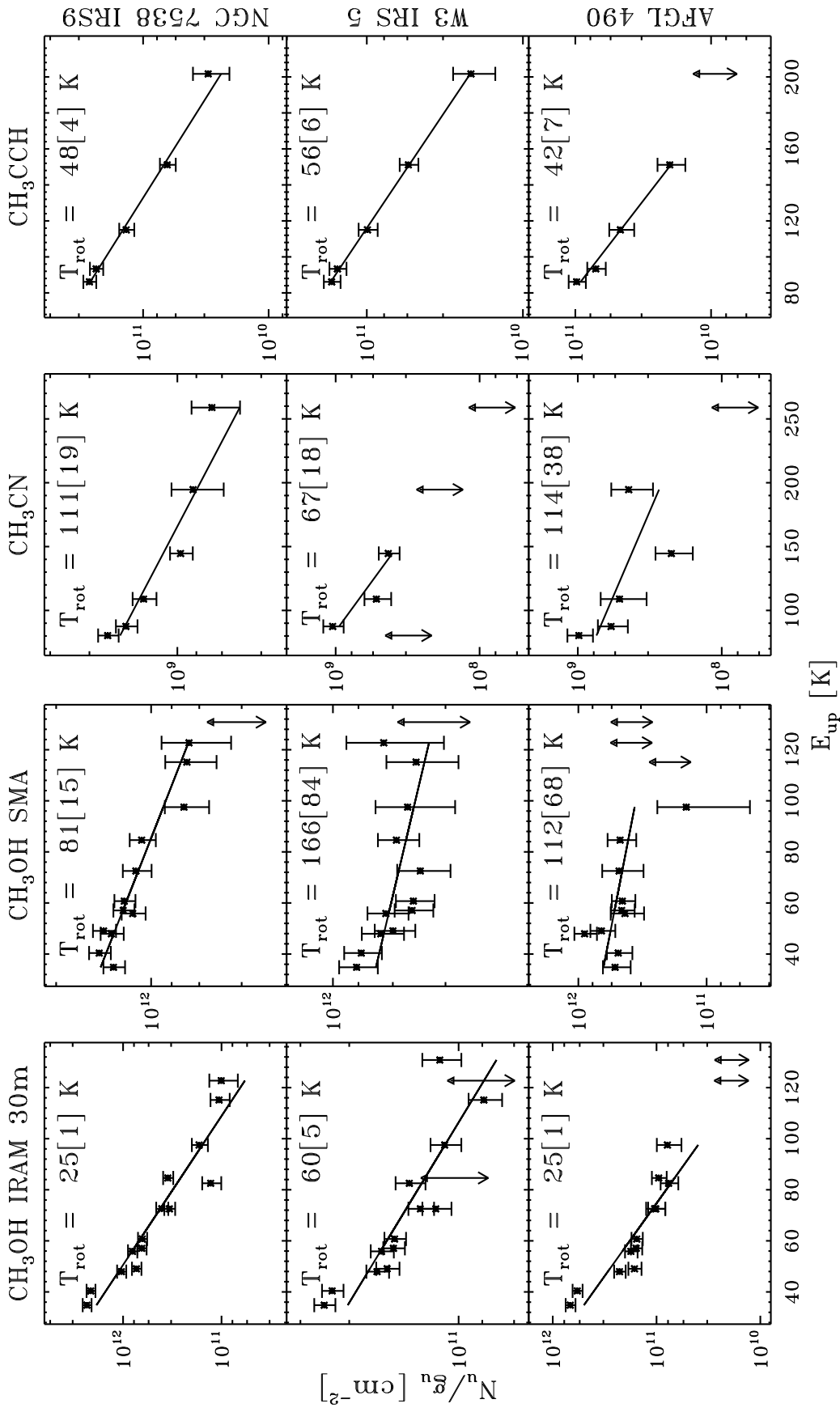


Figure 7.6: Rotational diagrams of CH₃OH from the single dish data (first column), for CH₃OH from the SMA spectra extracted with a 2" mask (second column), and CH₃CN from the single dish data (third column), and CH₃CCH (fourth column) and for the sources NGC7538 IRS9 (first row), W3 IRS5 (second row), and AFGL490 (third row).

Table 7.7: Rotational temperatures and column densities for CH₃OH, CH₃CN, and CH₃CCH derived from the rotational diagrams presented in Fig. 7.6.

Species	NGC7538 IRS9		W3 IRS5		AFGL490	
	T _{rot} (K)	N (cm ⁻²)	T _{rot} (K)	N (cm ⁻²)	T _{rot} (K)	N (cm ⁻²)
CH ₃ OH (IRAM)	25 ± 2	9 ± 1 × 10 ¹⁴	64 ± 6	3.2 ± 0.4 × 10 ¹⁴	25 ± 2	2.4 ± 0.4 × 10 ¹⁴
CH ₃ OH (SMA)	81 ± 16	2.5 ± 0.4 × 10 ¹⁵	166 ± 84	2.4 ± 0.5 × 10 ¹⁵	102 ± 67	1.2 ± 0.5 × 10 ¹⁵
CH ₃ CN ^b	111 ± 20	7 ± 2 × 10 ¹³	92 ± 23	2.4 ± 0.8 × 10 ¹³	164 ± 78	3.6 ± 1.2 × 10 ¹³
CH ₃ CCH	47 ± 5	1.2 ± 0.3 × 10 ¹⁵	58 ± 8	7 ± 2 × 10 ¹⁴	42 ± 7	4.2 ± 1.7 × 10 ¹⁴

^b Derived from IRAM 30m spectra rotational diagrams and applying a dilution factor corresponding to size the SMA 2'' mask radius over IRAM 10'' beam diameter.

Table 7.8: Column densities for HNCO, CH₃CHO, CH₃OCH₃ using excitation temperatures from Table 7.

Species	NGC7538 IRS9	W3 IRS5	AFGL490
	N (cm ⁻²)	N (cm ⁻²)	N (cm ⁻²)
HNCO _{ext}	4.0 ± 1.3 × 10 ¹³	1.8 ± 0.3 × 10 ¹³	6.0 ± 2.2 × 10 ¹²
HNCO _{comp}	1.1 ± 0.3 × 10 ¹⁴	1.4 ± 0.6 × 10 ¹⁴	< 4 × 10 ¹³
CH ₃ OCH ₃	3.3 ± 1.0 × 10 ¹⁴	9.7 ± 4 × 10 ¹³	4.5 ± 1.9 × 10 ¹⁴
CH ₃ CHO	3.1 ± 0.4 × 10 ¹³	< 1.1 × 10 ¹³	< 1.3 × 10 ¹³

7.3.4 Organics in hot core vs weak-line MYSOs

Per definition the line-poor MYSOs reported in this study have less intense emission of complex organic molecules compared to traditional luminous hot core sources. The question for this section is whether the chemical composition with respect to CH₃OH is different between the two source families. The CH₃CN, CH₃CCH, HNCO, CH₃CHO, and CH₃OCH₃ abundances with respect to CH₃OH obtained here for the three MYSOs are compared to the hot core abundances derived by Bisschop et al. (2007) in Figure 7.7. For the 3 MYSOs sources, the molecular abundances with respect to CH₃OH are calculated using the CH₃OH column densities derived for the envelope if the molecule has been classified as 'envelope' molecules and using the CH₃OH column density derived for the core (SMA-based) in the case of a core molecule. For the hot core sources, Bisschop et al. (2007) applied a dilution factor corresponding to the region where T > 100 K for CH₃OH, CH₃CN, HNCO and CH₃OCH₃, but not for CH₃CCH and CH₃CHO. To calculate CH₃CCH and CH₃CHO abundances with respect to CH₃OH we removed the dilution factor for CH₃OH applied by Bisschop et al. (2007). All other abundances are taken directly from Bisschop et al. (2007).

The histograms in Figure 7.7 show that the CH₃CN, CH₃OCH₃, and HNCO core abundances with respect to CH₃OH are similar for the young MYSOs and the hot-core sources. In contrast, the young MYSOs show higher envelope abundances with respect to CH₃OH compared to the hot core sources. This difference is most likely due to that we could not separate CH₃OH core and envelope emission in the study by Bisschop et al. (2007), resulting in artificially low envelope ratios with respect to CH₃OH when all CH₃OH is implicitly assumed to originate in the envelope; in reality

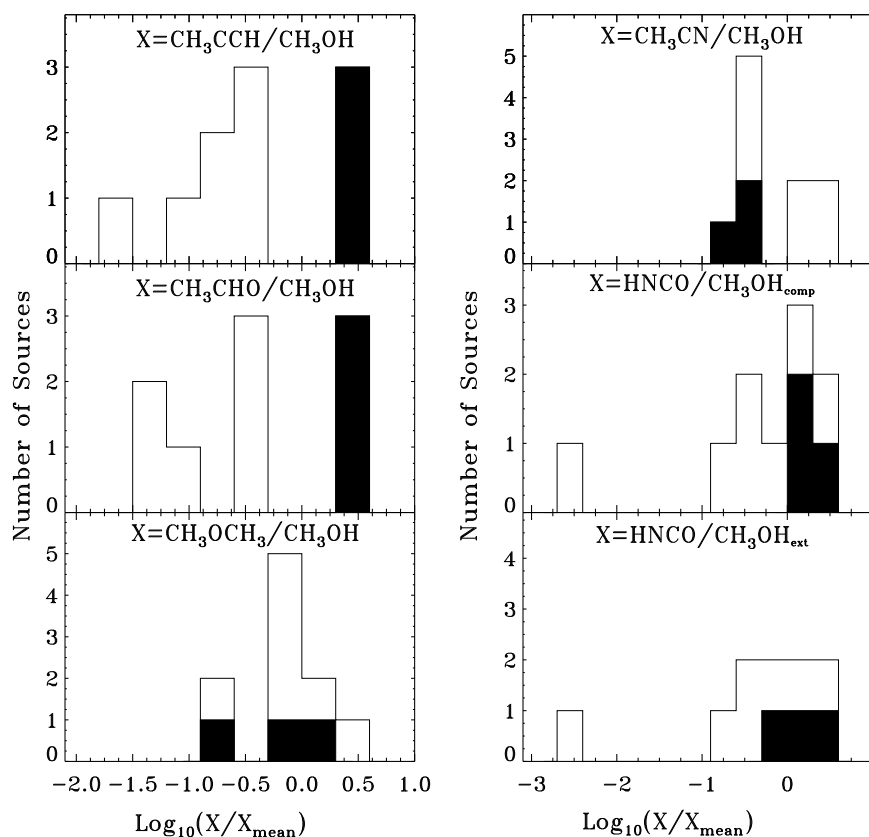


Figure 7.7: The solid filled histograms correspond to sources observed and analyzed here, the black contour histograms correspond to sources from Bisschop et al. (2007)

the high excitation temperature of CH_3OH in the hot core sources suggest that most of it really comes from the core.

Some of the same trends are visible for the log-log correlations of molecular abundances with respect to CH_3OH showed in Figure 7.8. In addition, these plots show that there is no clear correlation between the two N-bearing organics CH_3CN and HNCO and ratios span about one order of magnitude. There is also no correlation between the two O-bearing complex species CH_3OCH_3 and CH_3CHO , which is consistent with their different origins in the MYSOs. In contrast, there seems to be a correlation between envelope molecules CH_3CHO and CH_3CCH , but this potential trend is probably exaggerated by the different abundance derivations with respect to CH_3OH for the hot cores and the weak-line MYSOs.

7.3.5 An ice-gas connection?

The CH_3OH ice content may be an important factor on whether a hot core chemistry developed and we therefore compare the CH_3OH core column density toward weak-line MYSOs and hot cores with their CH_3OH ice abundance with respect to H_2O (Gibb et al. 2004) (see Table 7.1). In the hot cores the majority of the CH_3OH gas originates from the core and we use the derived column densities from Bisschop et al. (2007),

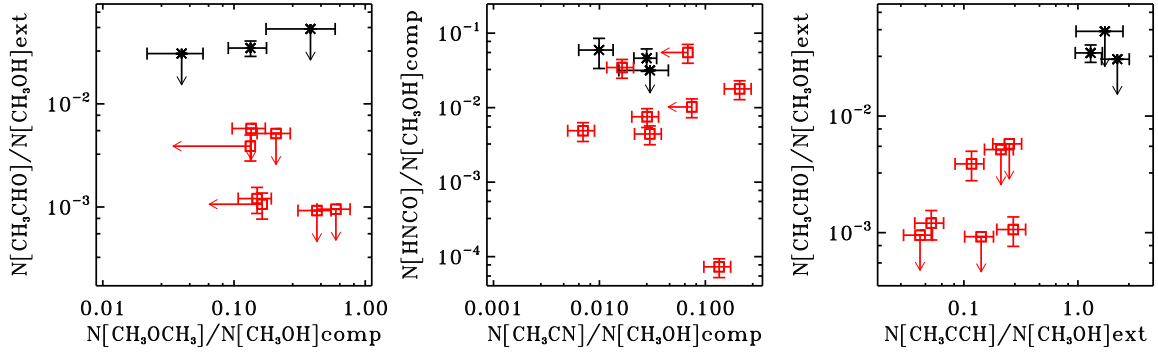


Figure 7.8: Gas abundance correlation between organics including upper limits. The black crosses are the abundances derived for the MYSOs, the red squares are derived by Bisschop et al. (2007). An arbitrary error of 20% has been taken for the latest values.

where all CH_3OH emission is assumed to originate from the central region where the temperature is higher than 100 K. For the MYSOs studied here, the regions where the temperature is higher than 100 K is derived using a relation between luminosity and temperature $R_{T=100\text{K}} \approx 2.3 \times 10^{14} (\sqrt{L/L_\odot})$, which was shown by Bisschop et al. (2007) to approximate the 100 K radius well toward their source sample. We further assume that all SMA CH_3OH line flux originate from these regions, based on the derived rotational temperatures, and use an appropriate dilution factor when the 100 K area is smaller than the $2''$ mask used for spectral extraction. Figure 7.9 presents the resulting column density of hot CH_3OH gas versus the initial CH_3OH abundance on the grains. No strong correlation is observed but more sources with information on the spatial distributions of CH_3OH are needed to reach a conclusive answer on the importance of the initial CH_3OH abundance.

The initial ice composition may also affect the complex organic composition in both hot cores and weak-line MYSOs. Figures 7.10 presents correlation plots between ratios of the N-bearing organics and CH_3OH in the ice and gas-phase. The two gas-phase N-bearing organics are HNCO and CH_3CN , and the two ice species are OCN^- and NH_3 . The ice abundances are listed in Table 7.1 and have been obtained by Gibb et al. (2004). A limited sample of 7 MYSOs have overlapping ice and gas observations. Moreover, only a fraction of them can be used in each plot due to multiple ice abundance upper limits. The top left panel of Figure 7.10 shows a tentative correlation between OCN^- ice and HNCO in the gas phase with respect to CH_3OH (the outlier is due to HNCO in the AFGL 490 envelope, while all other points trace HNCO in the cores). HNCO and OCN^- are linked through efficient thermal reaction within the ice (van Broekhuizen et al. 2004), and the gas-phase $\text{HNCO}/\text{CH}_3\text{OH}$ ratio may simply reflect the ice abundance ratio before evaporation, and a correlation between the ice and gas ratios is thus expected. The top right panel of Figure 7.10 shows the gas phase abundance of HNCO over CH_3OH with respect to NH_3 , another N-bearing molecule that could play a role in the HNCO/OCN^- formation scheme because it is a major source of nitrogen in the ice (van Broekhuizen et al. 2004); and again a tentative correlation is observed. The

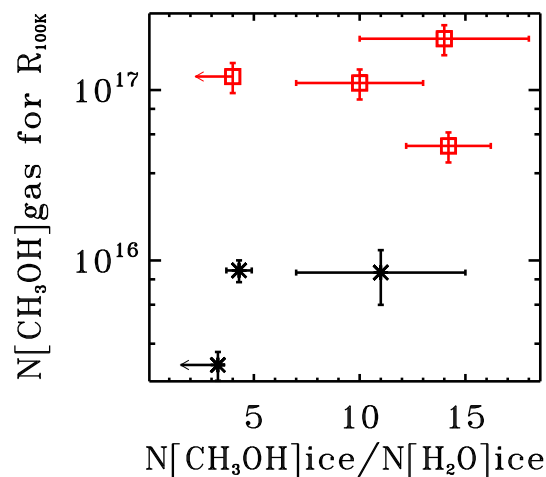


Figure 7.9: CH_3OH column density in the inner core versus CH_3OH ice abundance over H_2O ice in the envelope.

relation between OCN^- in the ice and CH_3CN in the gas is explored in the bottom left panel of Figure 7.10. These molecules are not correlated for the 4 sources presented here, despite both containing a CN functional group. Finally, the bottom right panel presents the $\text{CH}_3\text{CN}/\text{CH}_3\text{OH}$ gas ratio versus the $\text{NH}_3/\text{CH}_3\text{OH}$ ratio in the ice. There is no correlation, which is in contradiction with the predictions from Rodgers & Charnley (2001).

7.4 Discussion

7.4.1 Weak line MYSOs versus hot cores

Previous observations of complex molecules toward MYSOs have generally focused on sources with a well-developed hot core that is responsible for most of the molecular emission. In such cases either interferometric *or* single dish observations are sufficient to determine complex organic abundances as long as the radius of the evaporation front close to the central protostar is known. Single-dish observations combined with the rotational diagram technique can also be used to derive abundances of molecules that are pre-dominantly present in the outer envelope, since then beam-averaged abundances can be assumed. The real difficulty is the molecules that are distributed throughout the envelope and core. For such molecules, single-dish and interferometric observations need to be combined to deduce what fraction of the molecular emission originates in the envelope and in the core respectively, and then use these fractions to calculate the chemical composition of the two physically and chemically different regions. Based on this study, this class of molecules seems to mainly encompass 0th generation ices, i.e. CH_3OH and HNCO , but as our sensitivity increases we expect, based on model results, that many classical hot core molecules will present a

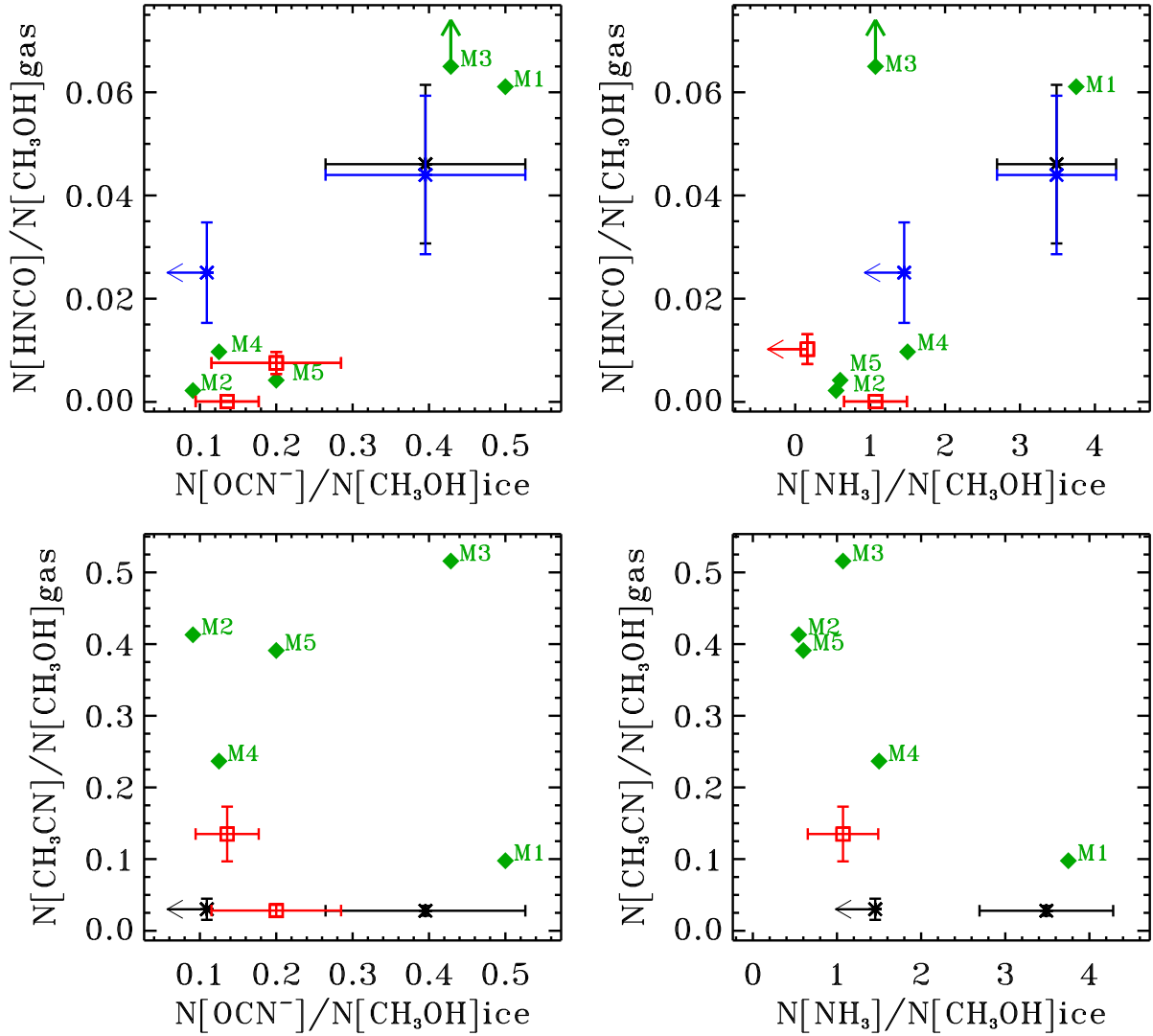


Figure 7.10: Ice versus gas abundance correlation for N-bearing species with respect to CH₃OH. The crosses are abundances derived respectively for the MYSOs, the red squares are the values derived by Bisschop et al. (2007). An arbitrary error of 20% has been taken for the latest values. For the two top plots the black crosses represent the HNCO over CH₃OH abundance derived for the compact component while the blue crosses correspond to the HNCO abundance calculation for an extended component. The green diamonds represent the model results for five initial abundance M1 to M5 reported in Table 7.9. The arrows for model M3 in the top panels are included to represent the high [HNCO]/[CH₃OH] abundance ratio of 0.3 in M3.

significant envelope emission profile as well.

Using the IRAM 30m and SMA spectra we could classify several complex organic molecules into belonging to the core, envelope and both. The two envelope molecules, CH_3CHO and CH_3CCH were similarly classified by Bisschop et al. (2007) based on excitation temperatures alone, suggesting that the envelopes around line-poor MYSOs and hot cores are chemically similar. In contrast we find that in the line-poor MYSOs, CH_3OH and sometimes HNCO have significant emission contributions from the envelope, while Bisschop et al. (2007) found that in hot core sources they have excitation temperatures above 100 K, and were thus classified as originating exclusively from the core region; these sources have probably a similar envelope line flux as observed for the line-poor MYSOs, but in single dish studies, this emission contribution is drowned out by the hot cores.

Overall, the chemistry in the young MYSOs is remarkably similar to what is observed in the hot cores, which suggests that they may be hot core pre-cursors. CH_3CN , CH_3CCH , CH_3CHO , HNCO , CH_3OCH_3 are observed in both kinds of sources at comparable abundances with respect to CH_3OH . $\text{CH}_3\text{CH}_2\text{OH}$ and HCOOCH_3 - two typical hot-core molecules - are not seen in the line-poor MYSOs, but typical abundance of these molecules with respect to CH_3OH from Bisschop et al. (2007) are consistent with non-detections. The hot-core pre-cursor interpretation is also consistent with the observed lack of CH_3OH core column density or hot-core activity on the initial CH_3OH ice abundance.

7.4.2 The ice-gas connection: Observations vs. Theory

Whether or not the overall hot-core chemistry depends on the initial ice composition, we expect that the ice composition will have an effect on the chemical composition in both hot cores and line-poor MYSOs. This dependence may look very different for complex molecules that form in the gas-phase from evaporated ices compared to products of complex ice chemistry. The fact that we do not observe a clear trend between NH_3 in the ice and CH_3CN in the gas suggests that the model of Rodgers & Charnley (2001) is missing important complex molecule formation pathways. We have therefore used the state-of-the-art *MAGICKAL* model (Garrod 2013) to explore the connection between ice and gas-phase species further. The model is based on rate-equations/modified rate-equations that treat the gas-grain chemistry by differentiating the gas-phase, the ice surface and the bulk of the ice.

We have run the *MAGICKAL* code for using the fiducial physical model from Garrod (2013), and a standard H_2O ice abundance, but varying the remaining ice composition to span the observed ranges in the combined line-poor MYSOs and hot cores sample (see M1 to M5 in Table 7.9). The resulting gas-phase abundance of HNCO , CH_3CN , and CH_3OH are reported at different temperatures during warm-up in table 7.10.

The relationships during protostellar warm-up between gas-phase HNCO and CH_3CN with respect to CH_3OH , and OCN- and NH_3 initial ice abundances with respect to CH_3OH ice are shown in Figure 7.11, for temperatures between 20 K and 100 K. Since the model does not treat ion chemistry in the ice, a full conversation rate

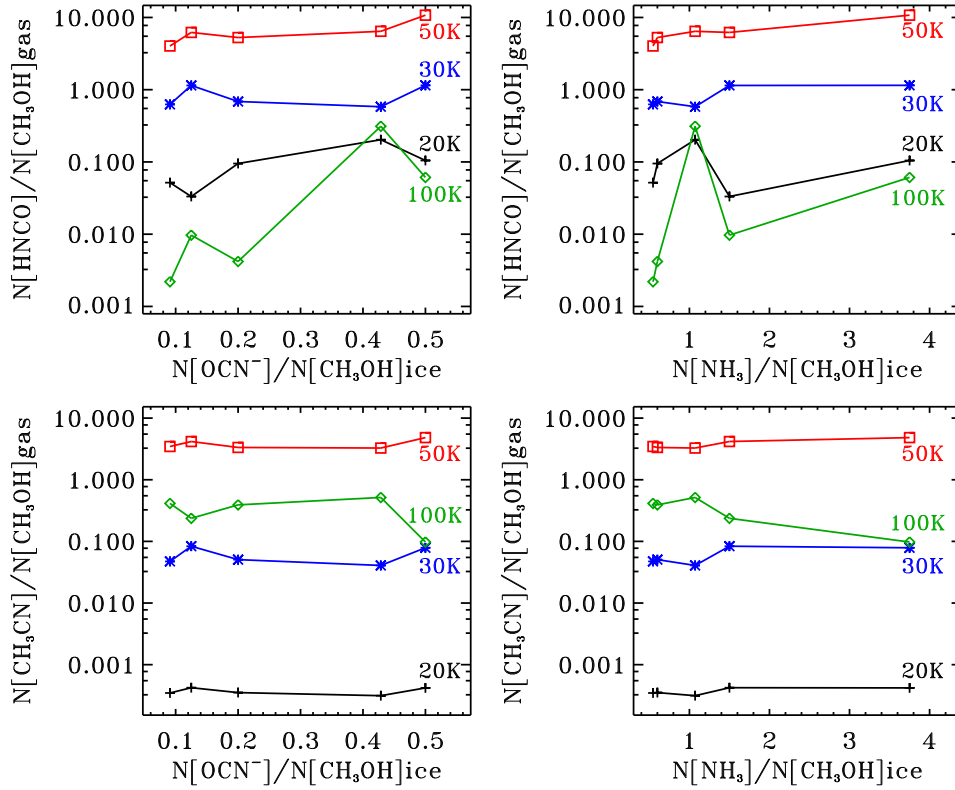


Figure 7.11: Model ice versus gas abundance correlation from the MAGICKAL model Garrod (2013). Five initial ice abundances are used to run the models and derived N-bearing abundances with respect to CH_3OH . The black plus signs present the results at 20 K, the blue crosses are the model results at 30 K, the red squares represents 50 K and the green diamonds are the results at 100 K.

Table 7.9: Initial ice abundances with respect to water used for the five chemical model simulation M1-5 . The three phase model assumes a H_2O abundance with respect to hydrogen of $2.66 \times 10^{-7} n_{\text{H}}$ for the ice surface and $1.46 \times 10^{-4} n_{\text{H}}$ for the ice bulk.

Species ratio	M1	M2	M3	M4	M5
$\text{CH}_3\text{OH}/\text{H}_2\text{O}$	4	11	14	4	10
$\text{CH}_4/\text{H}_2\text{O}$	2	2	2	2	2
$\text{HNCO}/\text{H}_2\text{O}$	2	1	6	0.5	2
$\text{NH}_3/\text{H}_2\text{O}$	15	6	15	6	6

of HNCO ice into OCN^- has been assumed based on the efficient HNCO to OCN^- conversion derived experimentally by van Broekhuizen et al. (2004). Figure 7.11 shows that both ice composition and temperature have strong impacts on gaseous abundance ratios and it is therefore clearly important to compare the simulation outputs and gas-phase observational data at similar gas temperatures.

Observationally, most HNCO and CH_3CN appears to originate at high temperatures and we therefore focus on the predictions at 100 K. The gas-phase abundances at 100 K derived from the simulations are over-plotted on the observational data in Figure

Table 7.10: Gas abundances with respect to hydrogen at various temperatures derived by the Garrod (2013) model for the initial ice abundances presented in Table 7.9

Model	Species	n(20 K)/n _H	n(30 K)/n _H	n(50 K)/n _H	n(100 K)/n _H
M1	CH ₃ OH	1.630×10^{-11}	1.082×10^{-12}	4.906×10^{-11}	3.165×10^{-9}
	HNCO	1.706×10^{-12}	1.243×10^{-12}	5.273×10^{-10}	1.933×10^{-10}
	CH ₃ CN	6.841×10^{-15}	8.522×10^{-14}	2.367×10^{-10}	3.092×10^{-10}
M2	CH ₃ OH	1.961×10^{-11}	1.880×10^{-12}	1.129×10^{-10}	6.814×10^{-9}
	HNCO	1.013×10^{-12}	1.177×10^{-12}	4.546×10^{-10}	1.497×10^{-11}
	CH ₃ CN	6.810×10^{-15}	8.898×10^{-14}	3.908×10^{-10}	2.814×10^{-9}
M3	CH ₃ OH	2.173×10^{-11}	2.617×10^{-12}	1.139×10^{-10}	7.291×10^{-9}
	HNCO	4.412×10^{-12}	1.521×10^{-12}	7.323×10^{-10}	2.272×10^{-9}
	CH ₃ CN	6.821×10^{-15}	1.065×10^{-13}	3.723×10^{-10}	3.761×10^{-9}
M4	CH ₃ OH	1.613×10^{-11}	9.645×10^{-13}	5.875×10^{-11}	3.724×10^{-9}
	HNCO	5.362×10^{-13}	1.104×10^{-12}	3.644×10^{-10}	3.611×10^{-11}
	CH ₃ CN	6.822×10^{-15}	8.053×10^{-14}	2.449×10^{-10}	8.813×10^{-10}
M5	CH ₃ OH	1.938×10^{-11}	1.828×10^{-12}	9.365×10^{-11}	6.373×10^{-9}
	HNCO	1.842×10^{-12}	1.254×10^{-12}	4.935×10^{-10}	2.671×10^{-11}
	CH ₃ CN	6.829×10^{-15}	9.242×10^{-14}	3.127×10^{-10}	2.492×10^{-0}

7.10. The first thing to note is that the model predictions generally agree with observations within a factor of a few. Furthermore, the model predicts a correlation between OCN⁻ in the ice and warm HNCO in the gas phase with respect to CH₃OH, which is in agreement with observations. The relatively high HNCO/CH₃OH gas-phase abundance, compared to the initial ice abundance, in AFGL490 envelope is consistent with model predictions at lower temperatures.

The link between gas-phase HNCO and NH₃ ice is also suggested by the model except for the M3 run. The reason M3 deviates is not fully understood and a more in-depth theoretical study is required to explore the expected scatter in this relationship. In contrast to what has been proposed by Rodgers & Charnley (2001), the abundance of CH₃CN with respect to CH₃OH does not correlate with the NH₃ ice content in the MAGICCAL code output, and neither does the cyanide ice related species OCN⁻. This agrees with the observational results and is most likely due to CH₃OH is involved in the formation of CH₃CN.

Figure 7.10 presents an encouraging agreement between theory and observations, but currently both the explored model parameter space and the observational sample are small. The case is complicated further by indications from both theory and observations that gas-phase abundance ratios depend strongly on both the initial ice composition and the local temperature. A large sample of spatially-resolved gas-phase observations together with ice observations of the same object is therefore needed to conclusively establish how the complex gas-phase chemistry depends on the ice composition. As shown here, line-poor MYSOs contain detectable amounts of complex organic material and present a similar chemistry to hot cores. Most MYSOs with ice observations from ISO could therefore be used to expand the sample. SOFIA could potentially also be used to expand the sample of MYSO ice sources. In addition, a larger

grid of simulations is necessary to investigate systematically the theoretical impact of the different ice components on the gas-phase species and identify ice-gas correlations that should be tested observationally.

7.5 Conclusions

1. We detect complex organic molecules CH_3CN , CH_3CCH , CH_3CHO , CH_3OCH_3 together with HNCO and CH_3OH toward three young MYSOs without any previous evidence for hot-core activity.
2. Using a combination of single dish and interferometry observations, we find that CH_3CN and CH_3OCH_3 emission originates in the central core region, CH_3CHO and CH_3CCH in an extended envelope, and CH_3OH , and sometimes HNCO , have both envelope and core emission components.
3. The inferred molecular emission locations are consistent with rotational temperatures derived from the single dish observations, except for CH_3OH , where single-dish data are dominated by the envelope.
4. The abundances of complex organics with respect to CH_3OH in the warm core regions are indistinguishable for the line-poor MYSOs and the sample of hot core sources from Bisschop et al. (2007). The envelope chemistry also seems similar for both kinds of sources, but this analysis is limited by a lack of CH_3OH envelope data toward the hot core sources.
5. The OCN^- (and possibly NH_3) ice abundances seem to affect the $\text{HNCO}/\text{CH}_3\text{OH}$ gas-phase abundances. This relationship is reproduced by the *MAGICKAL* astrochemical code, assuming fiducial collapse and warm-up rates and initial ice compositions that span the observed range. In contrast to earlier model predictions, the new model and observations show no correlation between OCN^- and NH_3 ice abundances and gas phase $\text{CH}_3\text{CN}/\text{CH}_3\text{OH}$ abundances.

